Supplement of Atmos. Chem. Phys., 26, 11583–11604, 2026
https://doi.org/10.5194/acp-26-11583-2026-supplement

Atmospheric Chemistry and Physics
Open Access
EGU

Supplement of

Drivers of Atmospheric Volatile Methylated Sulfur Variability Across the Southern Ocean and Antarctic Coast

Caleb Mynard et al.

Correspondence to: Caleb Mynard (caleb.mynard@csiro.au)

S1 PTR-ToF-MS Processing, Quantification and Analysis

All PTR-ToF-MS data were processed and analysed using Ionicon Data Analyzer 2.2.0.7 (IDA, Ionicon Analytik, Innsbruck, Austria, Müller et al. (2013)). Ambient data were background corrected by linear interpolation of all background measurements to match ambient data cycles and then subtracted to give background-corrected data for each analysed VOC. Background-corrected calibration curves derived the calibration factors of VOCs included in the calibration gas standards (slope = cps ppbV^{-1}), which were applied to cps data and converted to volume mixing ratio VOCs signals (ppbV). We detected MeSH, DMS and DMSO and distinguished each from their isobaric ions, as illustrated in Figure S1 and Table S2. Figure S19 demonstrates the stability of the instrument response throughout the voyage, illustrating examples of the zero signals and calibration factors applied to the DMS and MeSH measurements. The zero measurements of DMS and MeSH remained stable throughout the campaign, with mean signals of 5 $\pm$ 2 cps and 1 $\pm$ 0.5 cps, respectively. These background counts per second signals were negligible relative to ambient signals and were therefore unlikely to contribute substantially to the reported background-corrected VOC volume mixing ratio concentrations (Fig. S19).

Minimum detectable limits (MDL) and uncertainties were calculated following the methods described by (Dunne et al., 2018), which observes the Guide to Expression of Uncertainty in Measurement (JCGM, 2008) and the Law of Propagation of Uncertainty (Bevington et al., 1993). Briefly, Dunne et al. (2018) propagate uncertainty in the gas standard reference concentrations (ppb), gas standard flow rates (mL min^{-1}), ambient measurement signal (counts per second), and gas standard reference signal (counts per second) with an expanded relative uncertainty of the mean with a coverage factor of $k = 2$ (*i.e.,* 95 % level of confidence). Within this propagated uncertainty, we account for uncertainties in gas standard concentrations (5 %), gas standard flow via mass flow controllers (2 %), dilution gas flow via mass flow controllers (2 %), ambient ion signal (6 %), calibration gas ion signal (2 %), and calibration factor variability (relative standard deviation of 8 %). These independent uncertainty components were propagated in quadrature, resulting in an estimated combined relative measurement uncertainty of 11-12 % for all VMS species. DMS calibrations conducted over multiple calibration gas concentrations during the voyage were consistently linear (R^2 = 0.9988 $\pm$ 0.0007; slope = 518 $\pm$ 43 cps ppbV^{-1}). The between-calibration variability in calibration factors was included as an independent uncertainty term because ambient concentrations were calculated using the temporally nearest calibration factor (Fig. S19).

In lieu of direct calibrations for MeSH and DMSO during the MISO voyage, we applied a scaled calibration factor to these species in the same way first described for MeSH in Mynard et al. (2025). Briefly, the scaled calibration factor was determined from post-campaign calibrations in October 2025 at Kennaook/Cape Grim, Tasmania, Australia (KCG) with certified gas standards containing DMS, MeSH and DMSO using the same instrument and applied to the data as follows:

$$CF(x_{MISO}) = CF(DMS_{MISO}) \times \frac{CF(x_{KCG})}{CF(DMS_{KCG})} \quad (1)$$

where CF is calibration factor in counts per second (cps) per ppb^{-1} and x is either of MeSH/DMSO. Therefore, in the case of semi-quantifying DMSO based on limited calibration data acquired after the voyage, where $CF(DMS_{MISO})$ = 518 cps ppb^{-1}, $CF(DMSO_{KCG})$ = 114 cps ppb^{-1}, $CF(DMS_{KCG})$ = 669 cps ppb^{-1}, the calculated $CF(DMSO_{MISO})$ of 88 cps

ppb^{-1} was applied to ambient cps data to transform it to volume mixing ratio ppb (see Table S3 and Fig. S19 for campaign calibration factors). This DMSO:DMS instrument sensitivity of ($\sim$1:6) is similar to the work of Zang and Willis (2025) ($\sim$1:8). The PTR-ToF-MS sensitivity to VOCs can also be computed using the measured ion counts of protonated species and the collision rate constant for the proton transfer reaction (k-rate approach), which is related to the kinetic conditions of the PTR-ToF-MS drift tube (De Gouw and Warneke, 2007; Sekimoto et al., 2017). However, Figure S2 illustrates that using this method on average underestimates the DMSO volume mixing ratio by a factor of $\sim$4.5 compared to our data corrected by the scaled calibration factor. Between each calibration cylinder, acetone was a common reference compound, allowing us to compare instrument sensitivity across standards. Consistent with our previous observations (Mynard et al. 2025; Mynard et al., in prep), we found that concentrations derived using calibration standards and those estimated using the k-rate approach differed by approximately a factor of 1-5. This demonstrates the uncertainty associated with k-rate approach quantification and reinforces the importance of frequent calibrations using appropriate standards for accurate quantification of, in this study, VMS compounds. Similar discrepancies have also been reported for MeSH (see Mynard et al. 2025). Our calibration cylinders did not contain enough compounds spanning a sufficiently wide range of reaction rate constants to robustly establish instrument sensitivity as a function of the k-rate approach.

S2 Biogeochemistry Observations

Measurement of DMS/O/P concentrations were made using the Organic Sulfur Sequential Chemical Analysis Robot (OSSCAR) (Asher et al., 2015). Briefly, OSSCAR is a custom built, semi-autonomous purge-and-trap system configured to extract DMS from 10 mL seawater samples via nitrogen sparging onto a thermal desorption trap, and the eluted DMS is then separated from other volatiles by a gas chromatography column. Subsequent DMSP and DMSO sub-samples are converted to DMS separately via fast NaOH hydrolysis (Asher et al., 2015) and electrochemical reduction (McCulloch and Tortell, 2023), respectively. The electrochemical reduction procedure was adapted to use a 1 mL addition of 1.8mM $NiSO_4$ (Sigma Aldrich) catalyst to a 10 mL sample, which was determined to produce comparable performance under the 30 min reduction protocol described in McCulloch and Tortell (2023). DMS/O/P concentrations were quantified by a custom-built chemiluminescence detector coupled to OSSCAR, following similar methodology to Nagahata et al. (2013) (Figure S3).

This chemiluminescence system consisted of a Hamamatsu R1924A photomultiplier tube (PMT) interfaced to a 5 mL semi-spherical reaction chamber. The PMT was operated at 1200 V supplied by a Stanford Research Systems PS350 high voltage (HV) source. A 30 mL min^{-1} flow of the carrier gas (N_2; gas code 034) delivered the analyte to the reaction chamber through a 316 stainless steel hypodermic capillary (0.014" $\times$ 0.004" ID $\times$ 0.3 m length) interfaced to OSSCAR through 1/16" PEEK tubing, IDEX PEEK sleeves, and zero dead volume fittings. The ozone/air mixture required to initiate the chemiluminescence reaction was produced from an Enaly 1KNT ozone generator using zero grade air (gas code 055) and was supplied to the PMT reaction chamber through 1/16" PTFE tubing at 120 mL min^{-1}. The chemiluminescence signal produced from the system was then amplified using a Keithley 427 current amplifier using a 107-range gain and recorded with a digital acquisition device (DAQ; National Instruments) and a custom LABVIEW (National Instruments) program. Daily six-point calibration curves and

point standards were run on the coupled OSSCAR-chemiluminescence system to ensure satisfactory performance. Data analyte runs that had several peaks appear other than DMS were excluded, as they are likely to be other unknown sulfur compounds separated out by the gas chromatography column and detected by chemiluminescence. Intermittent or insufficient heating of the thermal desorption traps occurred during underway measurements, resulting in suspiciously high DMS/O/P concentrations. These data were excluded and explain the sparsity of data points shown in Figure S3.

Phytoplankton biomass community structure was determined through analysis of photosynthetic pigments using high performance liquid chromatography (HPLC) on samples collected from Conductivity, Temperature, Depth instrument (CTD) vertical profile deployments. The pigments were extracted and analysed according to Wright et al. (2010). Chemotaxonomic analysis of the pigments was then undertaken using a Shiny graphical user interface for the R package *phytoclass* (Hayward et al., 2023; Hayward et al.) which uses a simulated annealing algorithm to derive phytoplankton groups. To account for changes in pigment:Chl-*a* ratios under varying environmental conditions such as light and nutrient availability, hierarchical clustering was initially undertaken, which produced 3 groups sharing similar pigments. Based on previous studies in the Southern Ocean (Heidemann et al., 2024; Hayward et al., 2025, 2024; Wright et al., 2010), 8 phytoplankton taxa were included in the final analysis; Prasinophytes, Chlorophytes, Cryptophytes, Diatoms-2, Dinoflagellates-1, Haptophytes, Pelagophytes and Cyanobacteria. Relative composition of surface phytoplankton classes are presented in Figure S3 and vertical depth profiles of each phytoplankton class over case study regions (Mertz Polynya Area, Process Station 2 and Open Ocean) are shown in Figure S4. To support these biogeochemical studies, five Triaxus tows were conducted within proximity of the process stations to acquire vertical profiles of the ocean up to $\sim$200 m depths. Attached to the Triaxus hull was a chromophoric dissolved organic matter (CDOM) fluorometer which we employ to describe the CDOM vertical distribution across the case study regions, illustrated in Figure S10.

S3 Air Mass Back Trajectory Analysis

Figure S5 demonstrates that over the Antarctic Ice-Edge, DMS, MeSH, and DMSO exhibit stronger correlations with cumulative boundary-layer Chl-*a* (cBLChl-*a*) at shorter back-trajectory lengths, with the maximum sensitivity occurring at $\sim$6 hours. Whereas, correlations in the Open Ocean peak at longer time scales ($\sim$24 hours), reflecting the broader spatial influence and limited variability of both biological production and atmospheric transport processes offshore. Although correlations at 6 hours and shorter durations are expected to be higher for VMS, as these compounds have rapid emission–oxidation cycles, short atmospheric lifetimes, and are strongly influenced by immediate upwind biological conditions, very short back-trajectory windows can also overweight instantaneous variability. Therefore we employed 12-hour trajectories in our air mass categorisation, which also allowed us to more clearly distinguish geospatial extents of oceanic from Antarctic air masses. All 12-hour trajectories and their associated air mass history/productivity classification are depicted in Figures S6 and S7.

S4 Nocturnal Boundary Layer Accumulation Flux Estimations

To evaluate how oceanic emissions contribute to the observed coupling and decoupling of VMS species, we estimated the sea–air flux of DMS and MeSH. Following previous studies (Marandino et al., 2007; Lawson et al., 2020; Rocco et al., 2025) we can estimate DMS and MeSH fluxes from nocturnal accumulation in the marine boundary layer using Equation 2. The interplay between emission and atmospheric processing is also reflected in the diurnal cycle of DMS and MeSH, which is characterized by maxima in the early morning prior to the maximum incoming solar radiation and then minima in the early afternoon/evening due to enhanced photochemical loss from the presence of OH radicals. The main DMS/MeSH nighttime photochemical loss pathway is via the nitrate radical, which are usually low in abundance in this context, meaning that at night DMS and MeSH will accumulate in the boundary layer which can be leveraged to estimate their sea–air fluxes.

$$F_{DMS/MeSH} = \frac{d[DMS/MeSH]}{dt} \times h_{MBL} \tag{2}$$

In Equation 2, $\frac{d[DMS/MeSH]}{dt}$ is the increase in DMS or MeSH concentrations over time in ng m^{-3} s^{-1}, h_{MBL} is the height of the marine boundary layer estimated from radiosonde soundings, and $F_{DMS/MeSH}$ is the flux of DMS or MeSH in ng m^{-2} s^{-1}. This calculation has inherent uncertainty in the assumptions of zero DMS/MeSH losses in the boundary layer at night, horizontal homogeneity, and zero fluxes at the top of the boundary layer (Marandino et al., 2007). Therefore, we selected scenarios with consistent linear increases in DMS/MeSH over several hours characterised by environmental conditions consisting of air masses with oceanic origin away from frontal zones or strong phytoplankton blooms, measured photosynthetically active radiation of 0 ME m^{-2} s^{-1}, low-moderate wind speeds ($<$15 ms^{-1}), high-pressure conditions with low mechanical turbulence, and away from storm tracks over the Southern Ocean, which would drive tropospheric entrainment and more uncertain boundary layer height estimation. Based on these criteria, we selected only periods during the I9S Transect as the biologically heterogeneous regions near the Antarctic Ice-Edge would drive heterogeneous DMS/MeSH surface emissions.

Our results in Table S1 demonstrate higher calculated fluxes than previous nocturnal accumulation flux estimates from austral summer studies over the Southwest Pacific Ocean: Rocco et al. (2025) reported DMS and MeSH fluxes of 7.75–38.33 ng m^{-2} s^{-1} and 0.26–2.98 ng m^{-2} s^{-1}, respectively, and Lawson et al. (2020) found similar ranges (DMS: 9.1–22.3 ng m^{-2} s^{-1}, MeSH: 1.9–3.2 ng m^{-2} s^{-1}). This also involved similar, but generally higher, MeSH:DMS ratio fluxes, because of our higher observed increases in DMS and MeSH over time (Table S1) compared to these previous studies, *e.g.,* MeSH: 5 ± 1 ppt h^{-1} and DMS: 27 ± 4 ppt h^{-1}, which were observed amid a phytoplankton bloom at Chatham Rise (44° S, 174–181° E).

S5 Incubation of Natural Seawaters in Deckboard Mesocosm Experiments

To more directly investigate the coupling between marine biogeochemistry and VOC emissions, on-board mesocosm experiments were conducted as follows, approximately following the methods described in Rocco et al. (2025). These experiments are the focus of future works and a full analysis is beyond the scope of this publication. However, as described below, the mesocosm headspace maintained negligible concentrations of atmospheric oxidants, and as such the ratios of VMS species and

their oxidation products observed in the experiments serve as vital lines of evidence for investigating the effects of ventilation versus atmospheric oxidation in the ambient dataset.

Unfiltered seawater was pumped from 5-7 m depth using a trace-metal clean tow fish system. The device was mounted from a boom off the RV *Investigator's* midship beyond its wake and towed at five knots. Seawater was pumped directly into two 2000 L polypropelene mesocosm tanks. The mesocosm lids were made of polymethyl methacrylate (PMMA); both the tanks and lids were lined with Tedlar film. Light transmission was PMMA-limited across all wavelengths. From post-voyage measurements of the light transmission properties of the PMMA lid, there was $\sim$90 % transmission at all visible light wavelengths 396-1100 nm with a substantial drop off to $<$1 % transmission into the UV beginning $\sim$395 nm to 200 nm, as has been documented before for this material (e.g., Martínez-García et al. 2022). These results indicate high transmittance of photosynthetic active radiation (PAR) and low transmittance of ultraviolet radiation into the headspace, supporting the conclusion that the mesocosm headspace approximated an oxidant-free environment. This conclusion is supported by ozone measurements, which were below detection limits at all times in the mesocosm headspaces.

Each tank was simultaneously filled approximately halfway using a two-way flow splitter linked to an all-plastic pump (A100, Wilden) with a trace-metal clean Teflon diaphragm. The mesocosms were filled at select locations during the MISO voyage. One of these sample collection periods corresponded to Process Station 2 (PS2, 64$\circ$ S, 132$\circ$ E). The two tanks were analysed simultaneously, with one tank used to investigate nutrient perturbations to underlying biology and the other acting as an unamended control. These results will be the subject of future works and all findings reported here originate from the control tank to which no nutrients were added. Tanks were supplied with approximately 15 Lmin^{-1} air sourced from the aerosol inlet mast (described in main text Section 2) via Teflon tubing and scrubbed of aerosols and reactive gases via a scrubber system including activated charcoal and potassium permanganate gas scrubbing materials (CP Blend, Purafil) followed by a HEPA filter to remove aerosols and scrubbing media dust. Air was continuously sampled from the mesocosm headspace into the Air Chemistry Lab via teflon lines at a flow rate slightly lower than the air supply flow rate, with the excess air supplied to the mesocosm headspaces discharged via 2 m Teflon vent lines. This design was selected to prevent backflow of deck air into the mesocosm headspace. A valve system enabled the PTR-ToF-MS and complementary gas instruments to sequentially sample from the scrubbed mesocosm air supply, the ambient VOC inlet, and the mesocosm headspace lines of each of the sample tanks, with the scrubbed air supply serving as a zero for the mesocosm headspace measurements. Headspace temperature and light were recorded using a HOBO Pendant system. Atmospheric DMS and MeSH measured in the headspace of the control mesocosm tank from seawater sampled at PS2 are illustrated in Figure S16.

Period (UTC)	Average ship lat (° S), lon (° E)	Boundary layer height (m)	DMS (ppt h^{-1})	MeSH (ppt h^{-1})	F_{DMS} (ng m^{-2} s^{-1})	F_{MeSH} (ng m^{-2} s^{-1})	$F_{MeSH:DMS}$ (ng m^{-2} s^{-1})
8 Feb 2024 14:30–20:00	57.49, 115.00	1088	36 ± 16	4 ± 3	15.41–48.59	0.13–5.82	0.008–0.198
16 Feb 2024 15:00–21:00	51.54, 115.01	1138	45 ± 32	18 ± 7	20.39–65.41	4.04–16.64	0.070–0.462
21 Feb 2024 14:00–21:00	48.99, 115.00	1288	76 ± 52	12 ± 8	41.67–123.83	3.21–17.48	0.056–0.241
Feb–Mar 2012 (Lawson et al., 2020)	44, 174–181	1135 ± 657	18 ± 8	4 ± 1	14.87–36.01	2.61–4.33	0.11–0.19
Mar 2020 (Rocco et al., 2025)	44, 174–181	670–1450	N/A	N/A	7.75–38.33	0.26–2.98	0.03–0.15

Table S1. Nocturnal marine boundary layer fluxes of dimethyl sulfide (DMS) and methanethiol (MeSH) estimated from data in this study and compiled from previous Southwest Pacific Ocean voyages (Lawson et al., 2020; Rocco et al., 2025). Fluxes (F_{DMS}, F_{MeSH}) are reported in ng m^{-2} s^{-1}, with ranges reflecting the uncertainty propagated from measured concentrations (ppt h^{-1}).

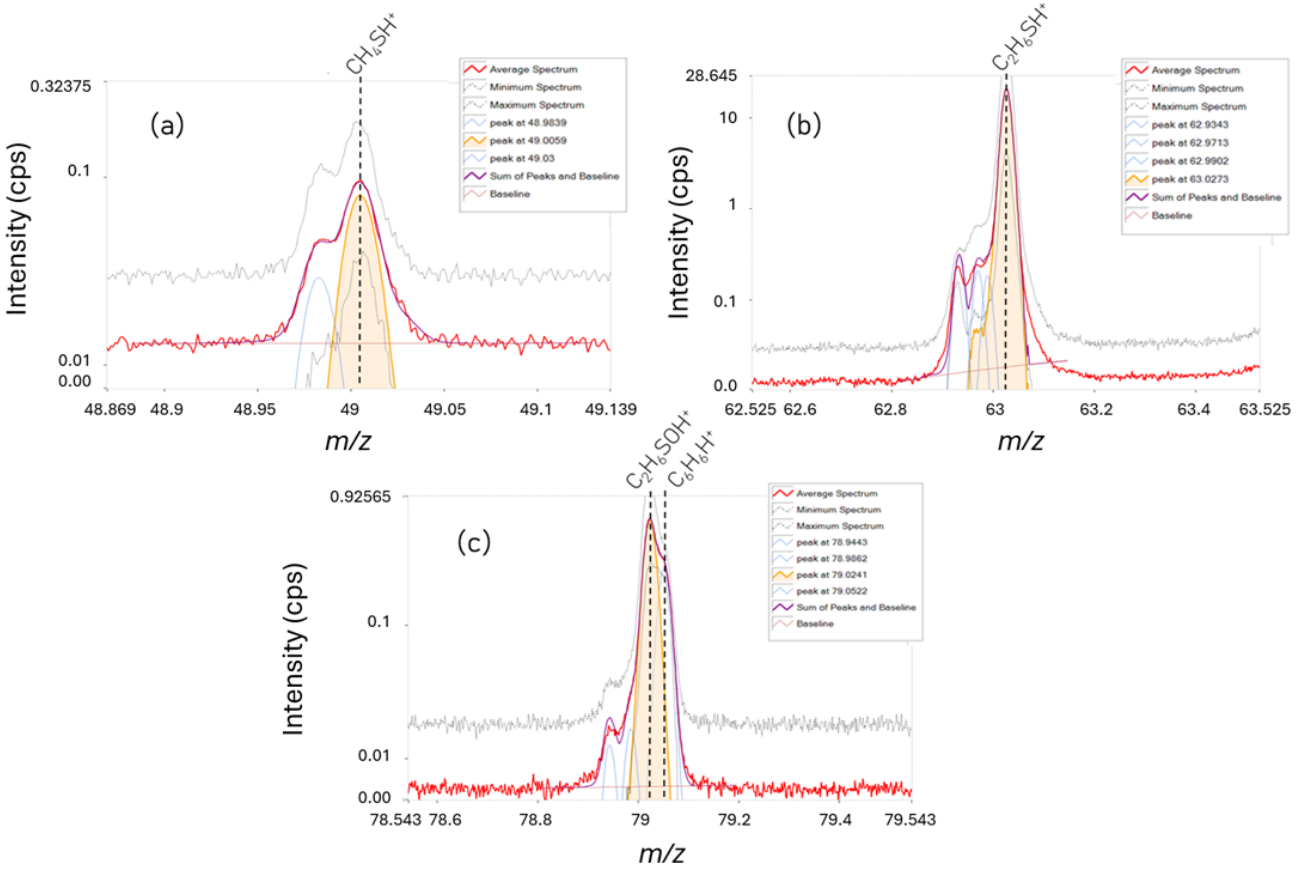

Figure S1. Ionicon Data Analyzer (IDA) detected ions and their peak systems for (a) methanethiol, (b) dimethyl sulfide and (c) dimethyl sulfoxide. The data period selected was during the extreme DMS event at the Mertz Polynya Area (13-01-2024).

Detected ion	Detected mass (Da)	Difference between ambient and calibration ion (mDa)	Chemical compound
CH_4SH^+	49.0059	0.88	Methanethiol
$C_2H_6SH^+$	63.0273	0.1	Dimethyl sulfide
$C_2H_6SOH^+$	79.0241	2.8	Dimethyl sulfoxide

Table S2. Detected VMS ions via PTR-ToF-MS during ambient and calibration measurements.

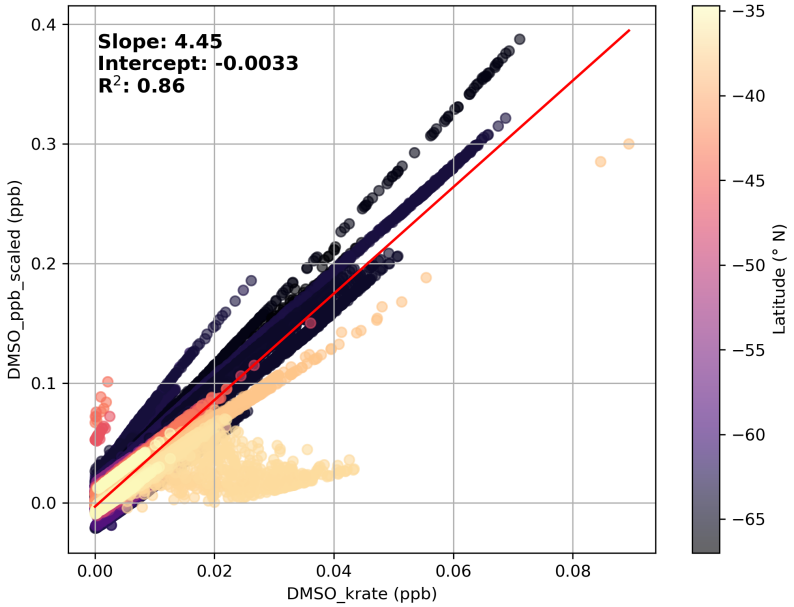

Figure S2. MISO ambient DMSO data comparing the method using an empirically derived scaling proxy (DMSO_ppb_scaled) and the proton-transfer collision-rate approach (DMSO_krate).

Table S3. Calibration factors of dimethyl sulfide (DMS), methanethiol (MeSH), and dimethyl sulfoxide (DMSO) in counts per second per parts per billion (cps ppbV^{-1}). Values are mean ± 1 standard deviation.

	KCGBAPS Sep–Dec 2023 (Mynard et al. 2025)	MISO Jan–Mar 2024 (This study)	KCGBAPS Apr 2024–Mar 2025 (Mynard et al. in prep.)
DMS (cps ppbV^{-1})	727.4 ± 34.6	518.3 ± 42.8	739.8 ± 57.3
MeSH (cps ppbV^{-1})	224.5 ± 10.7	159.9 ± 13.2	228.3 ± 17.7
DMSO (cps ppbV^{-1})	N/A	87.98 ± 6.97	N/A

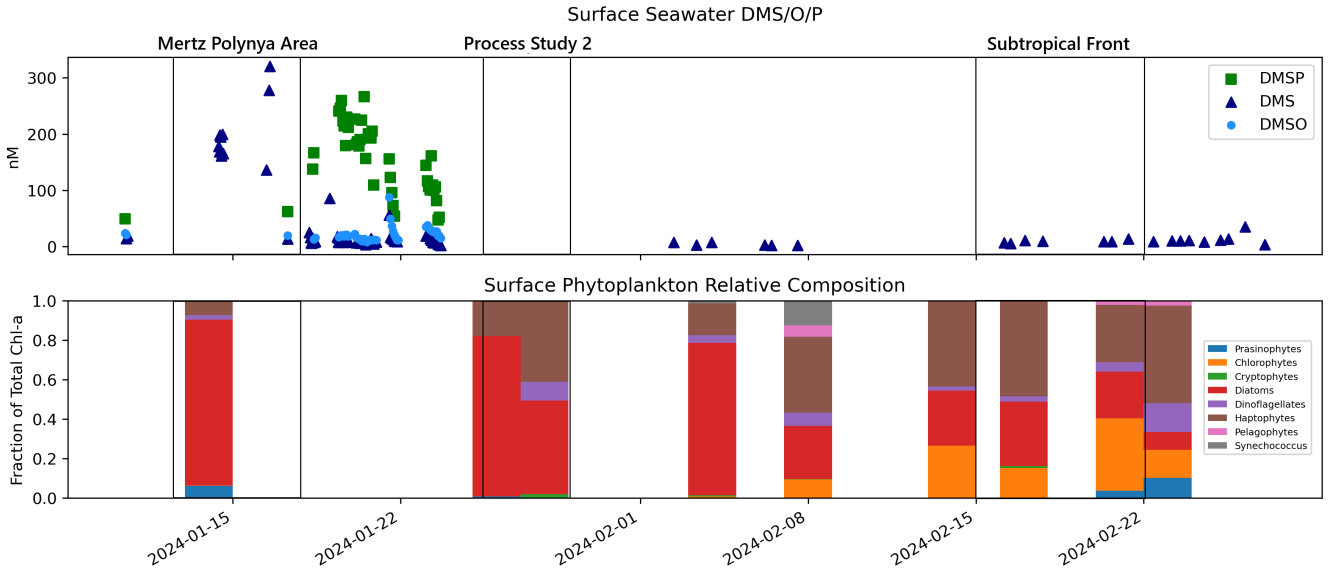

Figure S3. OSSCAR underway DMS/O/P measurements (7–23 Jan) and surface (5m) DMS taken from depth profiles along the I9S Transect (2–27 Feb) (top). Surface (∼3.5–15 m) phytoplankton class fraction of total Chl-*a* (bottom). Black vertical lines indicate case study periods discussed in the main text.

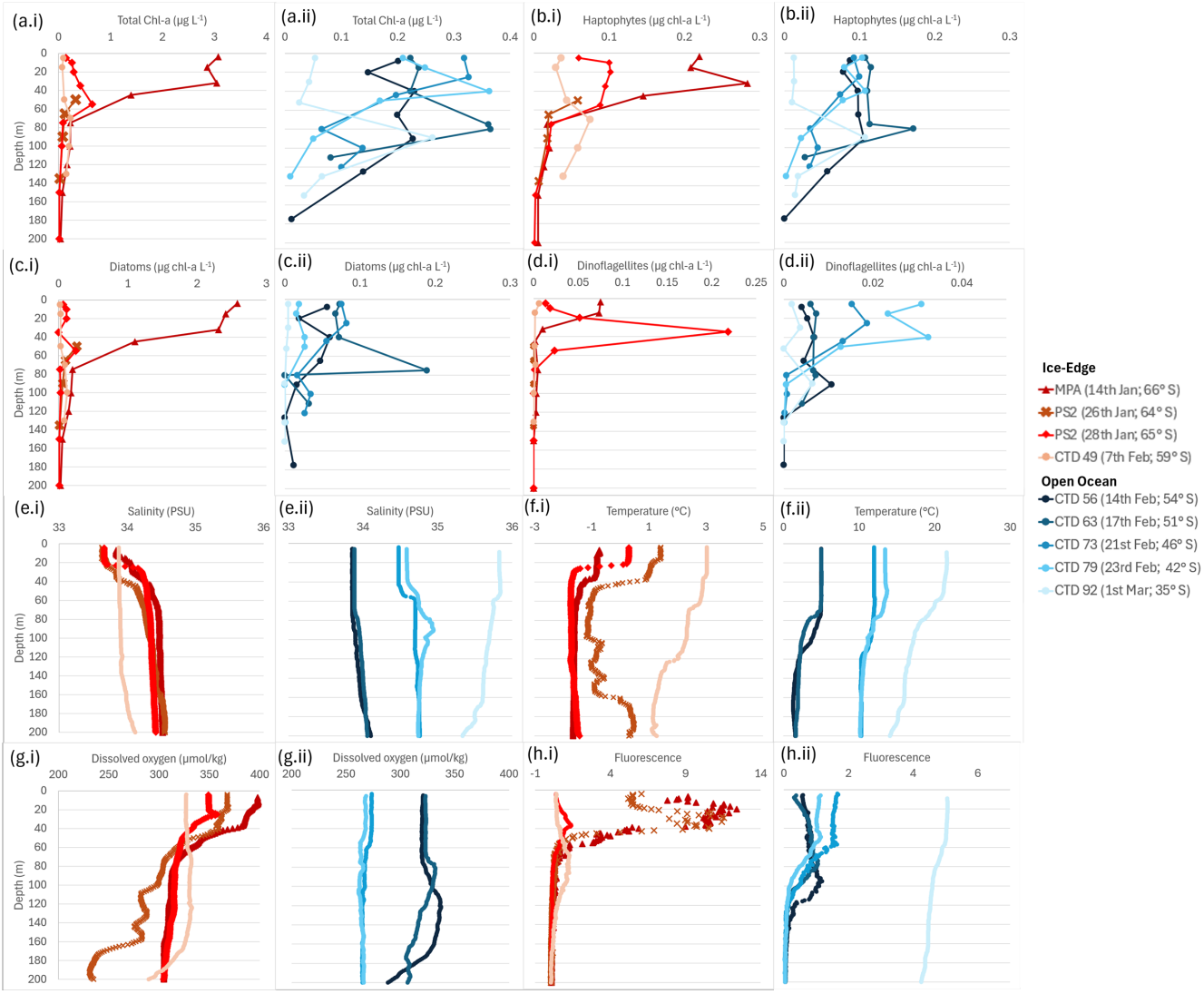

Figure S4. Depth profiles (0–200 m) of phytoplankton classes (a) Total Chl-a, (b) Haptophytes, (c) Diatoms, (d) Dinoflagellates, and (e) salinity, (f) temperature, (g) dissolved oxygen and (h) fluorescence from CTDs at the Antarctic Ice-Edge (i: Mertz Polynya Area, 65.33–67○S; Process Station 2, 64○S; CTD 49, 58.60○S) and over Open Ocean (ii: CTD 56, 54○S; CTD 63, 51.00○S; CTD 73, 46.01○S; CTD 79, 42○S; CTD 92, 35○S)

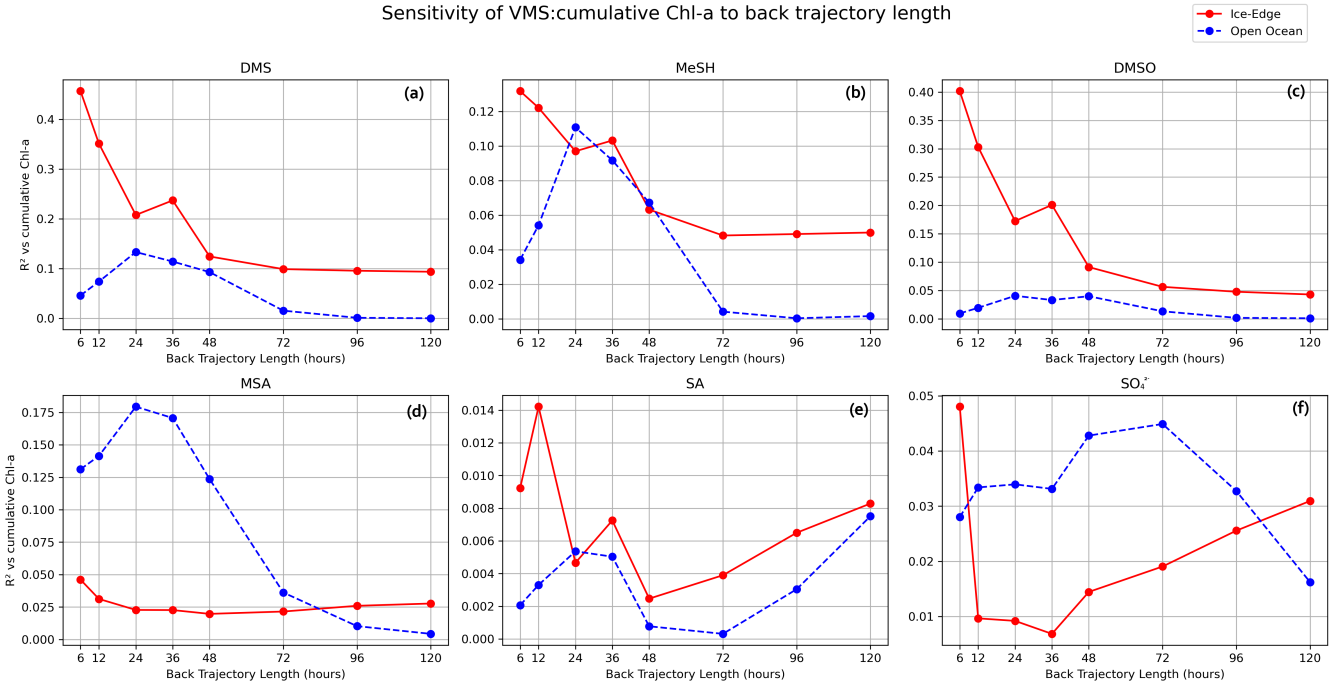

Figure S5. Coefficient of determination (R^2) between MODIS cumulative boundary layer chlorophyll-a and (a) DMS, (b) MeSH, (c) DMSO, (d) MSA, (e) SA, and (f) SO_4^{2-} aerosol over 6–120 hour back trajectory lengths. Red data are from the Antarctic Ice-Edge (<62°S) and blue data are from the I9S Transect Open Ocean (>62°S).

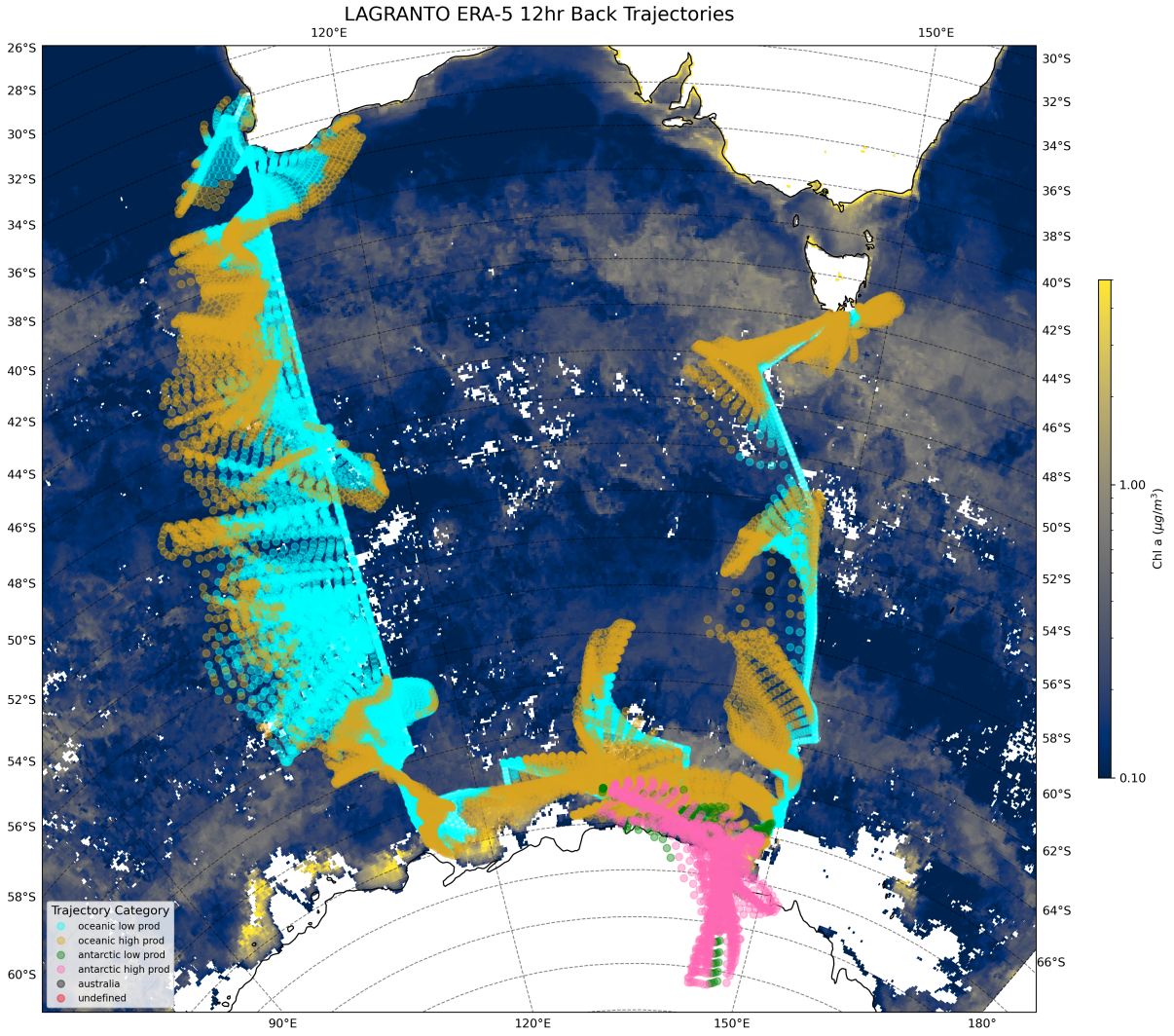

Figure S6. All 12-hourly LAGRANTO ERA-5 air mass back trajectories coloured by oceanic low productivity (cyan), oceanic high productivity (yellow), Antarctic low productivity (green), and Antarctic high productivity (magenta). Please refer to Fig. S15 indicating the locations of the three case studies.

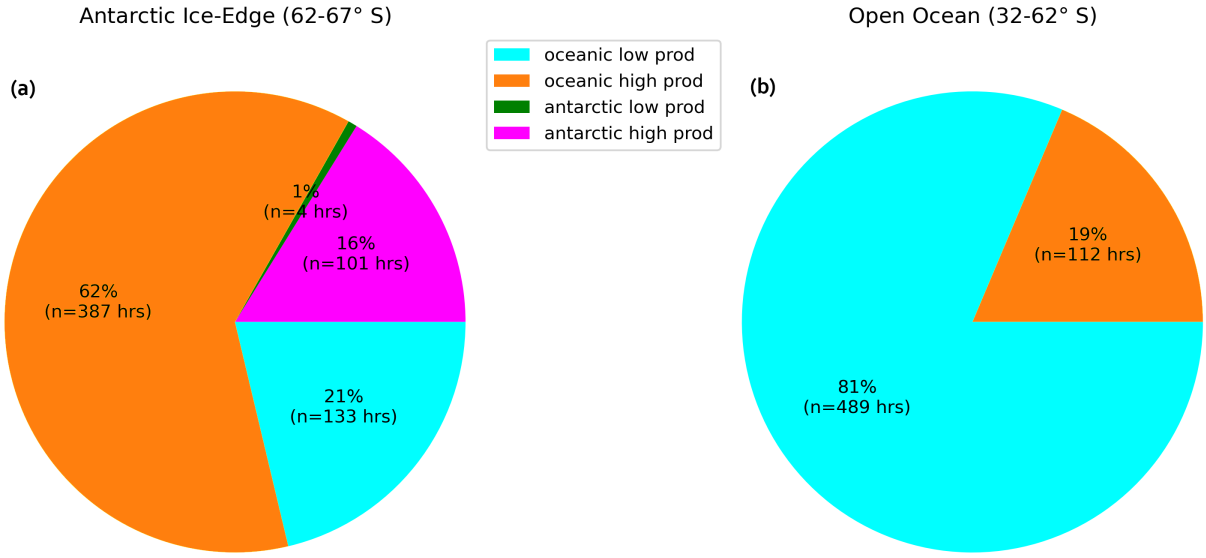

Figure S7. Relative contribution of each air mass classification to total sampled air masses over Antarctic Ice-Edge (left) and Open Ocean (right) spatial boundaries.

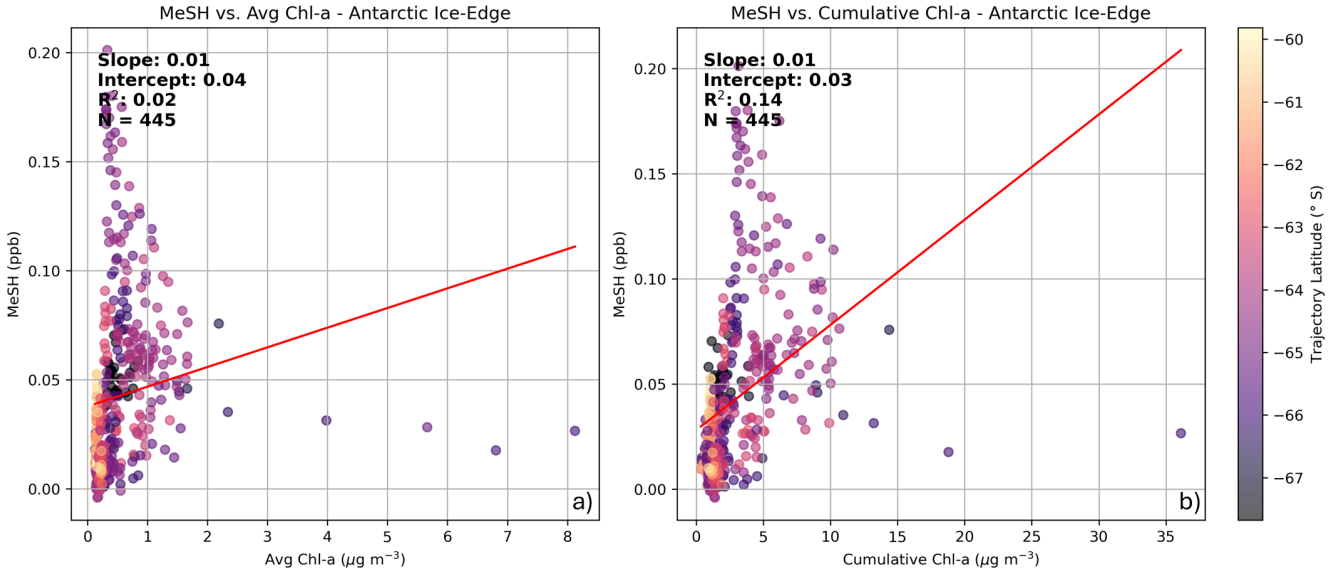

Figure S8. Scatterplots of MeSH versus back trajectory averaged Chl-*a* (a) and back trajectory cumulative Chl-*a* (b), coloured by back trajectory averaged latitude.

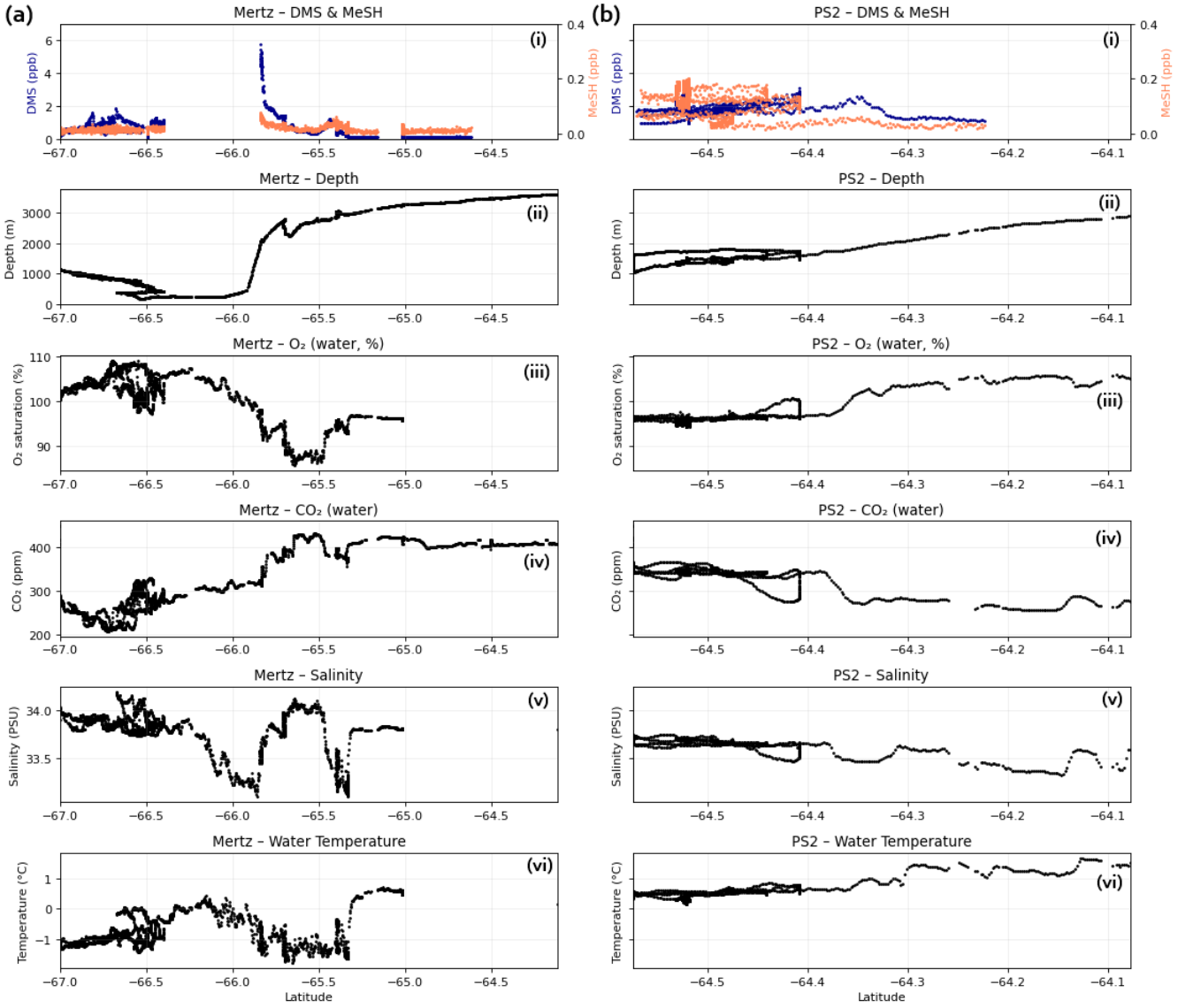

Figure S9. Underway observations of (i) atmospheric DMS and MeSH, (ii) seafloor depth, (iii) dissolved oxygen saturation, (iv) seawater fraction of CO_2, (v) salinity, (vi) sea surface temperature over the (a) Mertz Polynya Area (12–17 Jan 2024) and (b) Process Study 2 (26–28 Jan) case studies.

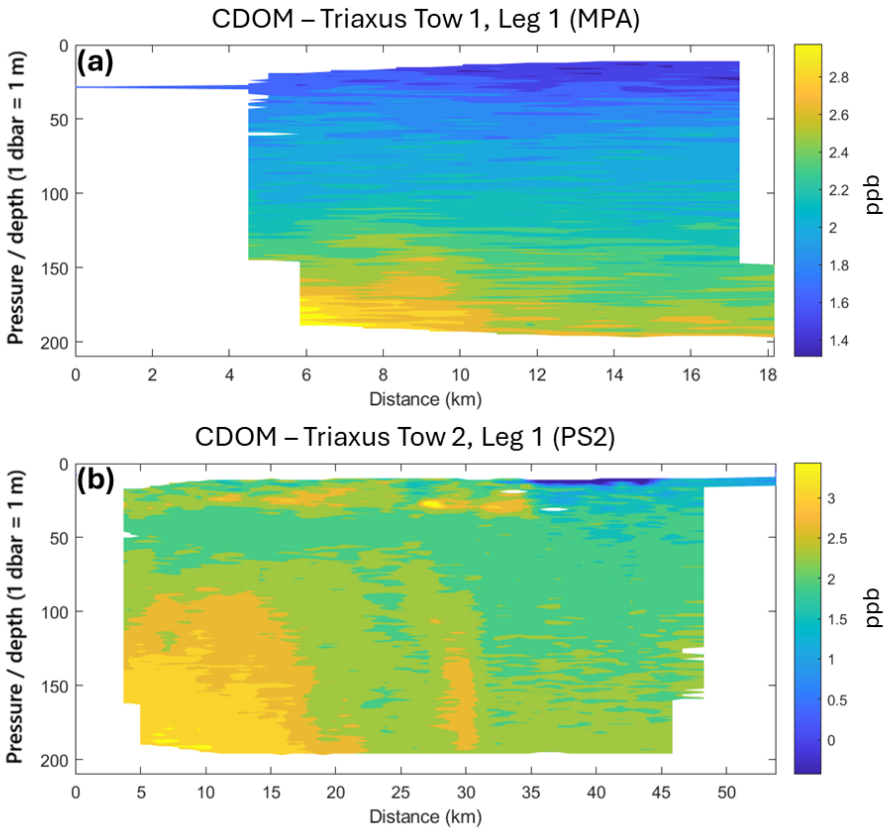

Figure S10. Chromophoric dissolved organic matter (CDOM) vertical profiles over Triaxus tows near the Mertz Polynya Area (a) and Process Station 2 (b). 1 dbar is approximately equivalent to 1 m in depth. The dataset IN2024_V01_TRIAXUS_plots.zip downloaded on 30-Dec-2025 was collected on RV Investigator voyage IN2024_V01. It is made available under a Creative Commons Attribution 4.0 International License (CC BY 4.0). We acknowledge the use of the CSIRO Marine National Facility, https://ror.org/01mae9353 in undertaking this research.

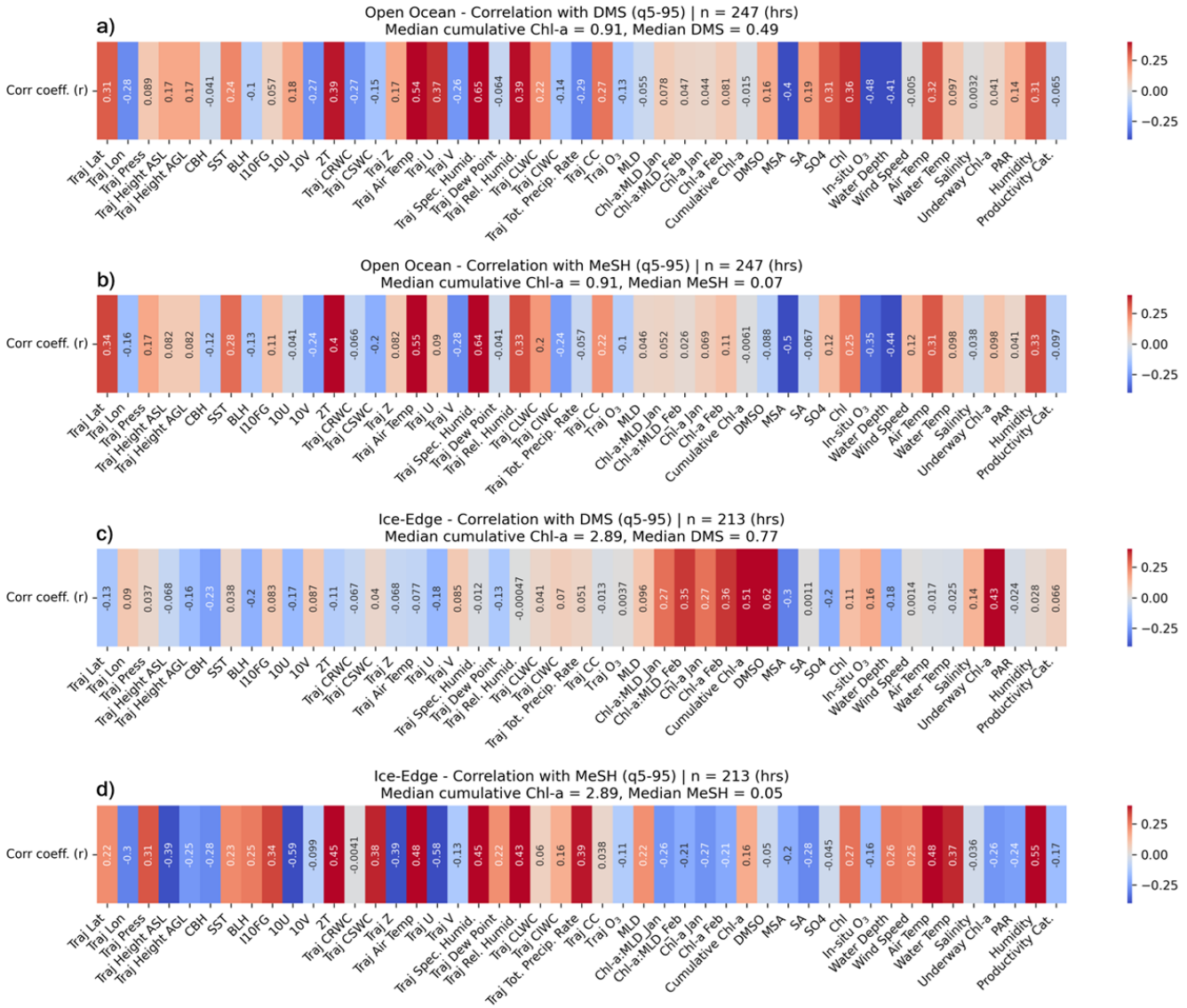

Figure S11. Pearson correlation coefficient (r) of 5th–95th percentile DMS (a, c) and MeSH (b, d) data versus measured and back trajectory parameters over Open Ocean (a, b) and Ice-Edge (c, d) regions.

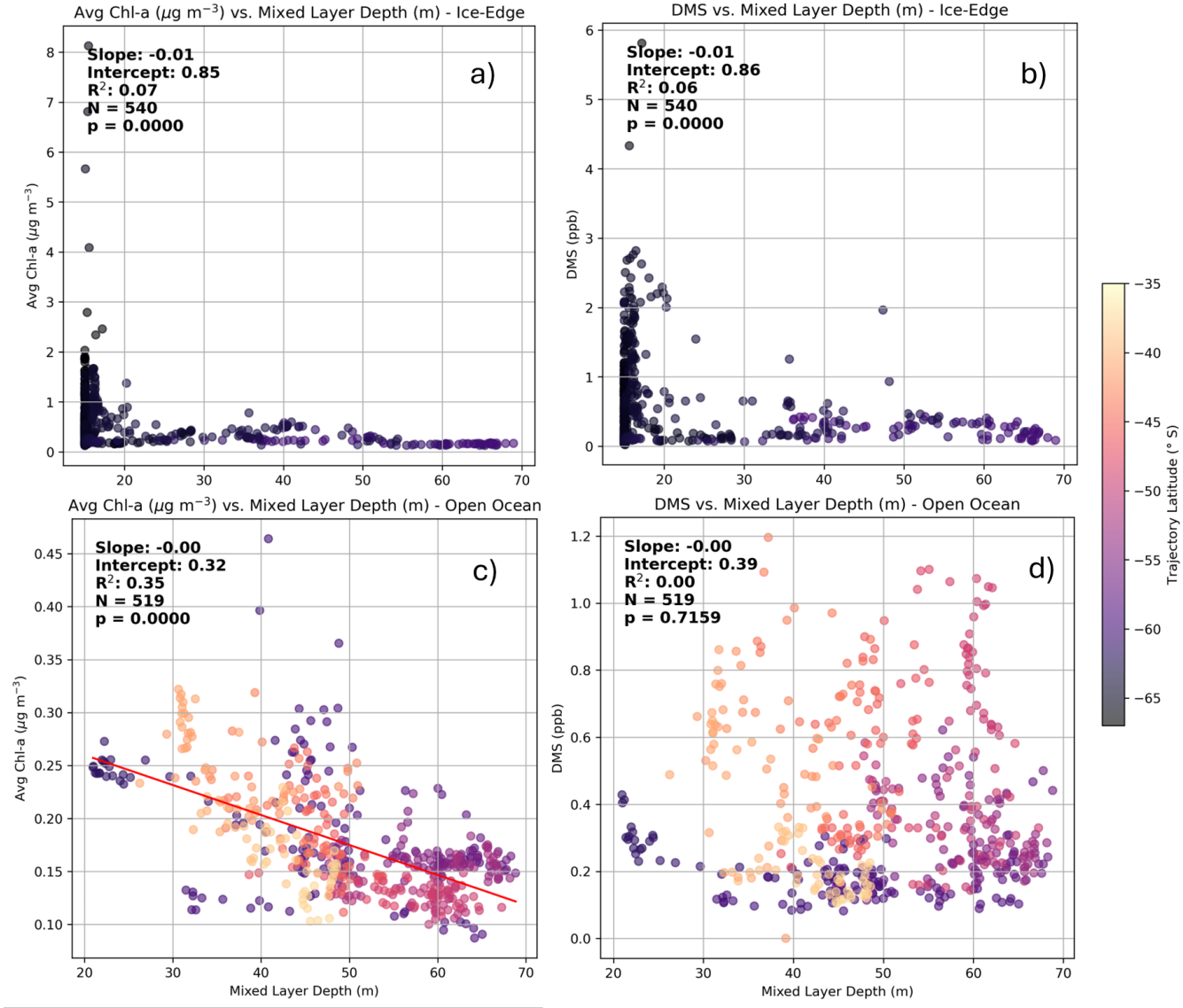

Figure S12. 12 hourly back trajectory averaged Chl-*a* versus mixed layer depth (MLD) and DMS versus MLD at the Antarctic Ice-Edge (a, b) and Open Ocean (c, d)

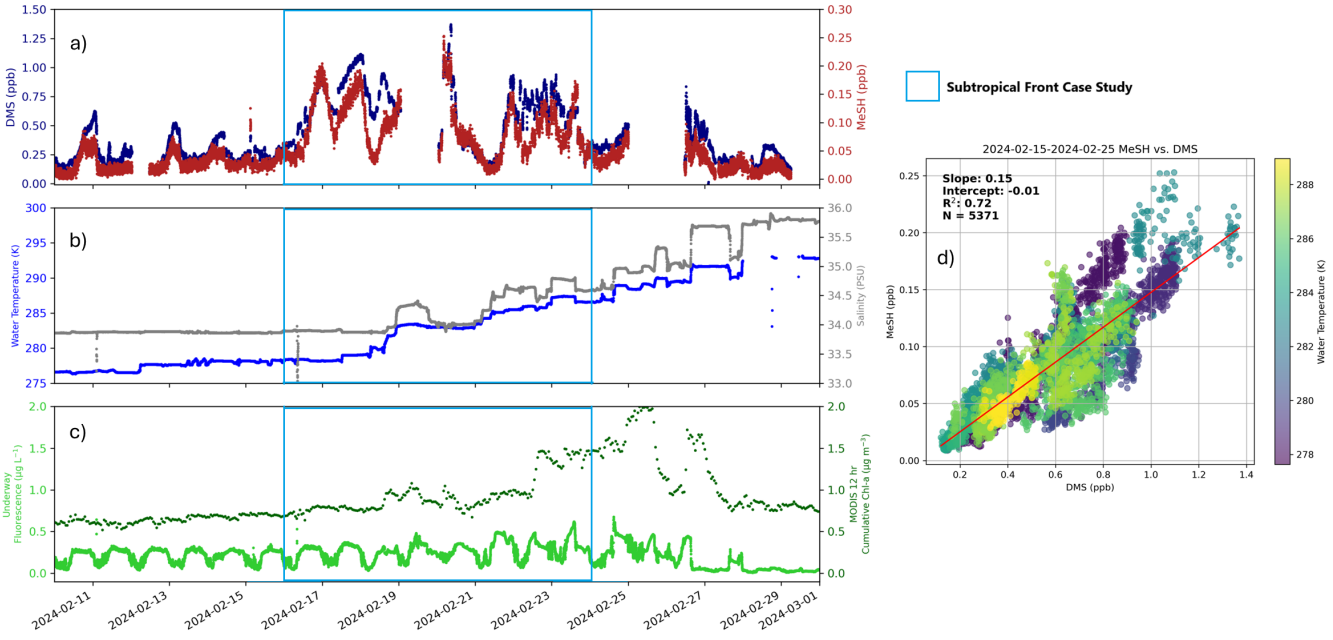

Figure S13. Observations near the subtropical front region (∼40–55°S; Feb 10–Mar 1 2024) of (a) atmospheric DMS (blue) and MeSH (red), (b) measured sea surface temperature (blue) and measured salinity (grey), (c) in-situ underway fluorescence (limegreen) and MODIS 12-hour cumulative boundary layer Chl-*a* (darkgreen), and (d) RMA regression between MeSH and DMS coloured by sea surface temperature over the Feb 15-25 period.

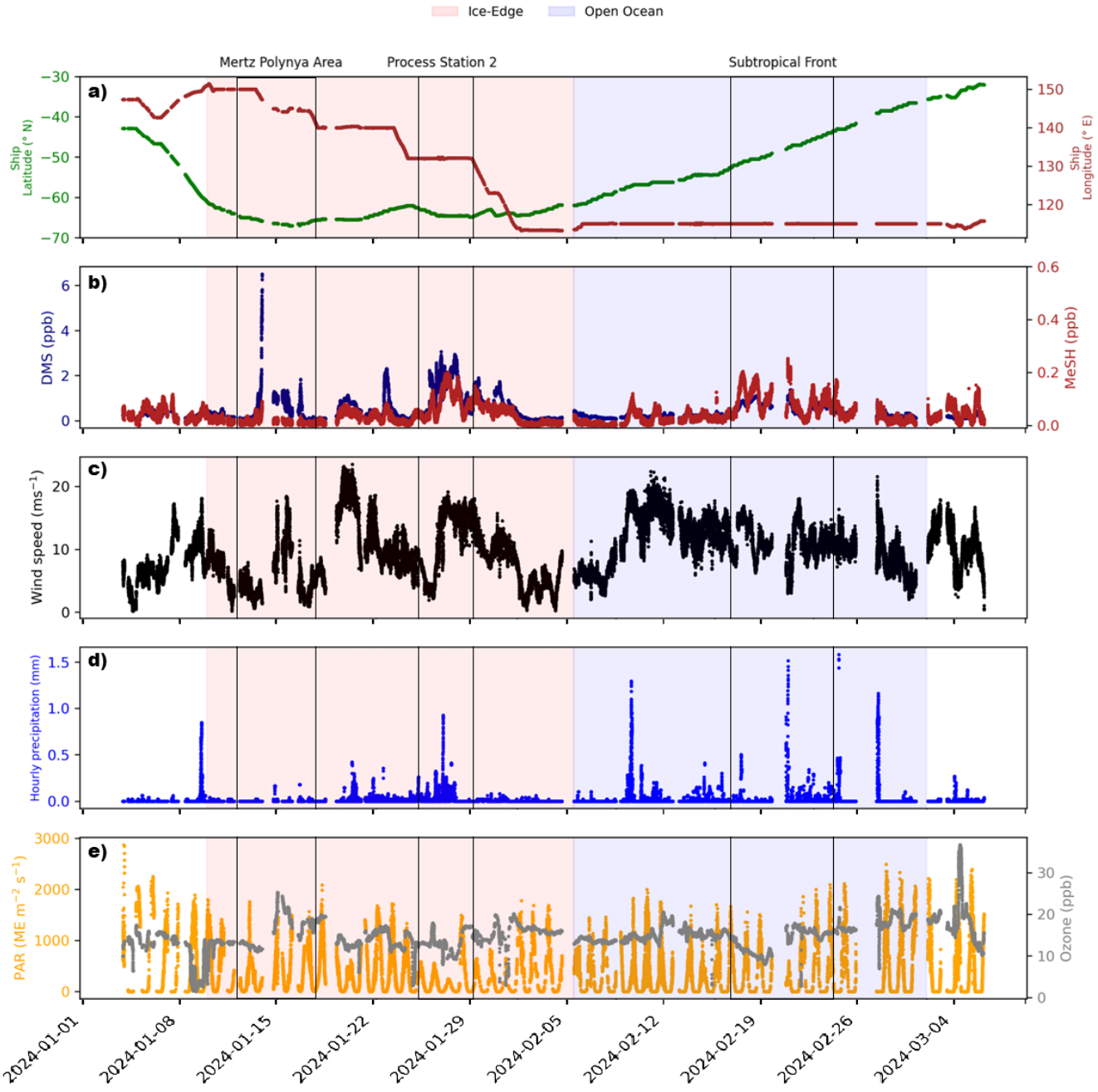

Figure S14. MISO voyage time series of *in-situ* measurements and derived product variables from satellite/model outputs. (a) *RV* Investigator ship latitude/longitude (green/brown), (b) gas-phase volume mixing ratio MeSH (dark red) and DMS (navy), (c) measured true wind speed, (d) measured hourly rainfall, and (e) measured ozone (grey) and photosynthetically active radiation (yellow). The highlighted red section indicates the Antarctic Ice-Edge region and the blue section indicates the Open Ocean (I9S Transect) region. Black vertical lines indicate case study periods discussed in the main text.

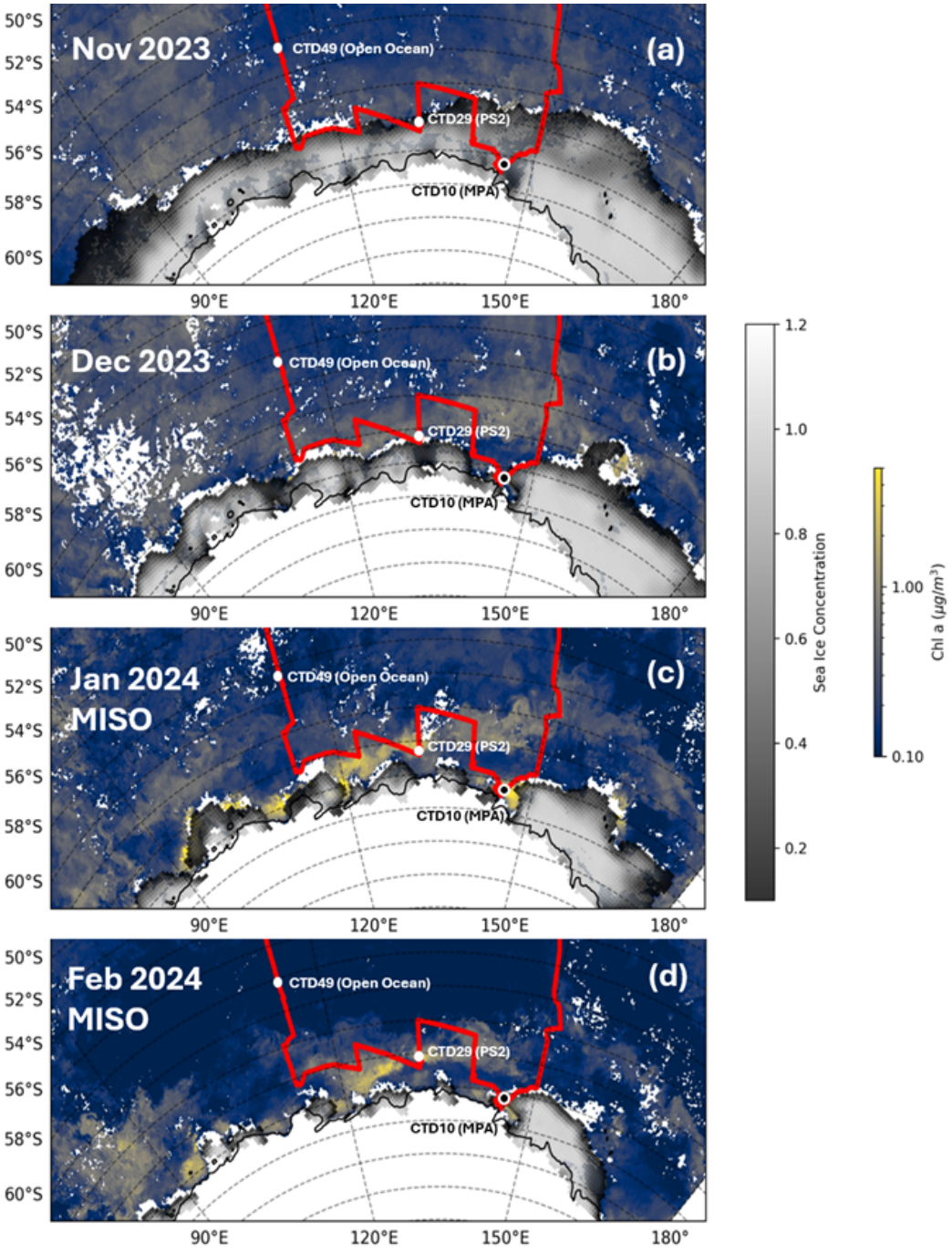

Figure S15. Monthly sea ice concentration from 25 km resolution National Snow and Ice Data Center (Sea ice concentration © NSIDC; Fetterer et al. 2025) and monthly MODIS Aqua Chl-a (MODIS Aqua Chl *a* © NASA Earth) satellite products over (a) Nov 2023, (b) Dec 2023, (c) Jan 2024, and (d) Feb 2024. Markers identify locations of CTD10 at Mertz Polynya Area, CTD29 at Process Station 2 and CTD49 over open ocean.

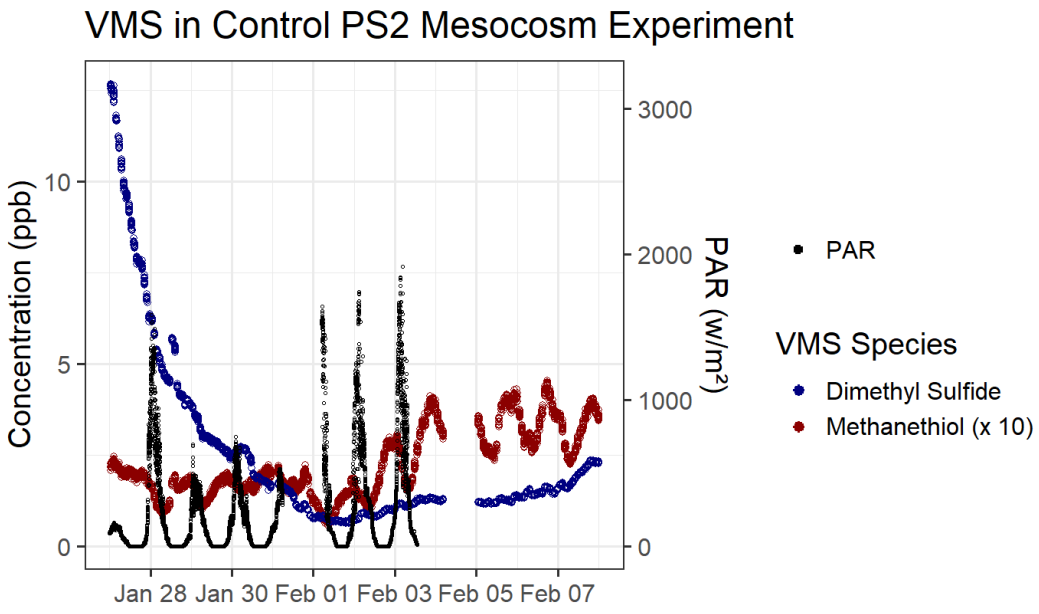

Figure S16. Volatile methylated sulfur (VMS) concentrations, dimethyl sulfide (navy) and methanethiol (red, $\times 10$ for visibility), measured in the headspace of the control (no nutrient addition) mesocosm tank from seawater sampled at Process Station 2 (PS2, 64° S, 132° E). Measured photosynethcially active radiation (PAR) is shown in black.

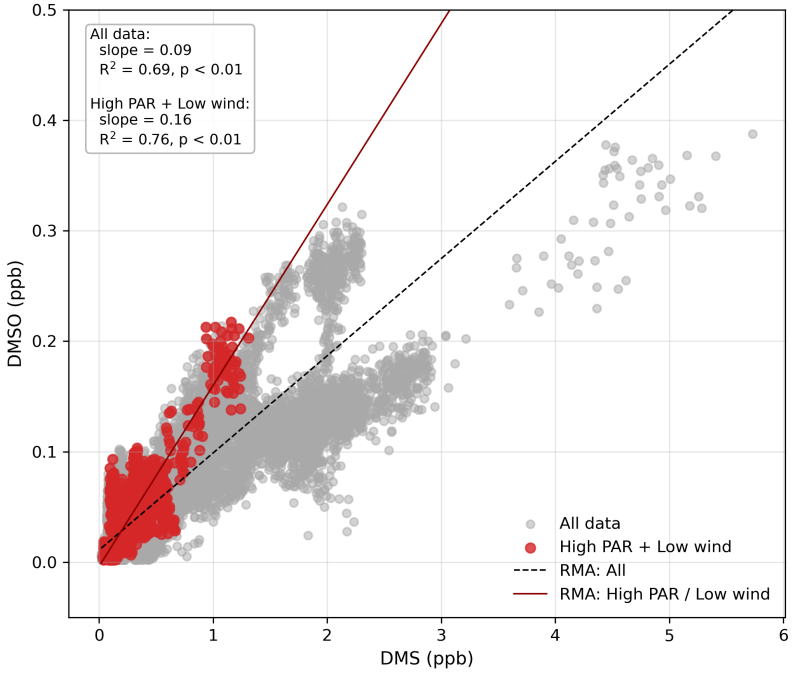

Figure S17. RMA regression scatterplots between DMSO and DMS at the Antarctic Ice-Edge under all conditions (grey) and under exclusively high photosynthetically active radiation (PAR >85th percentile: >700 μmol m^{-2} s^{-1}) / low-moderate in-situ wind speed (1-10 ms^{-1}) conditions (red).

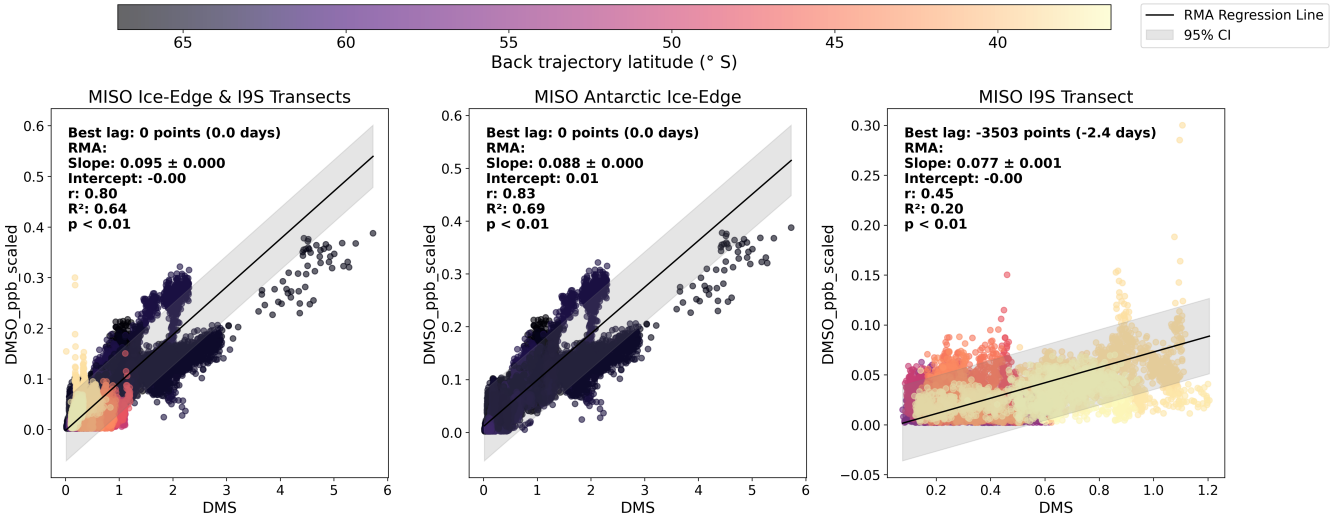

Figure S18. Time-lagged auto-correlated reduced major axis (RMA) regression scatterplots between 1-min measured DMSO and DMS constrained to (a) all MISO data, (b) Antarctic Ice-Edge, and (c) Open Ocean (I9S Transect).

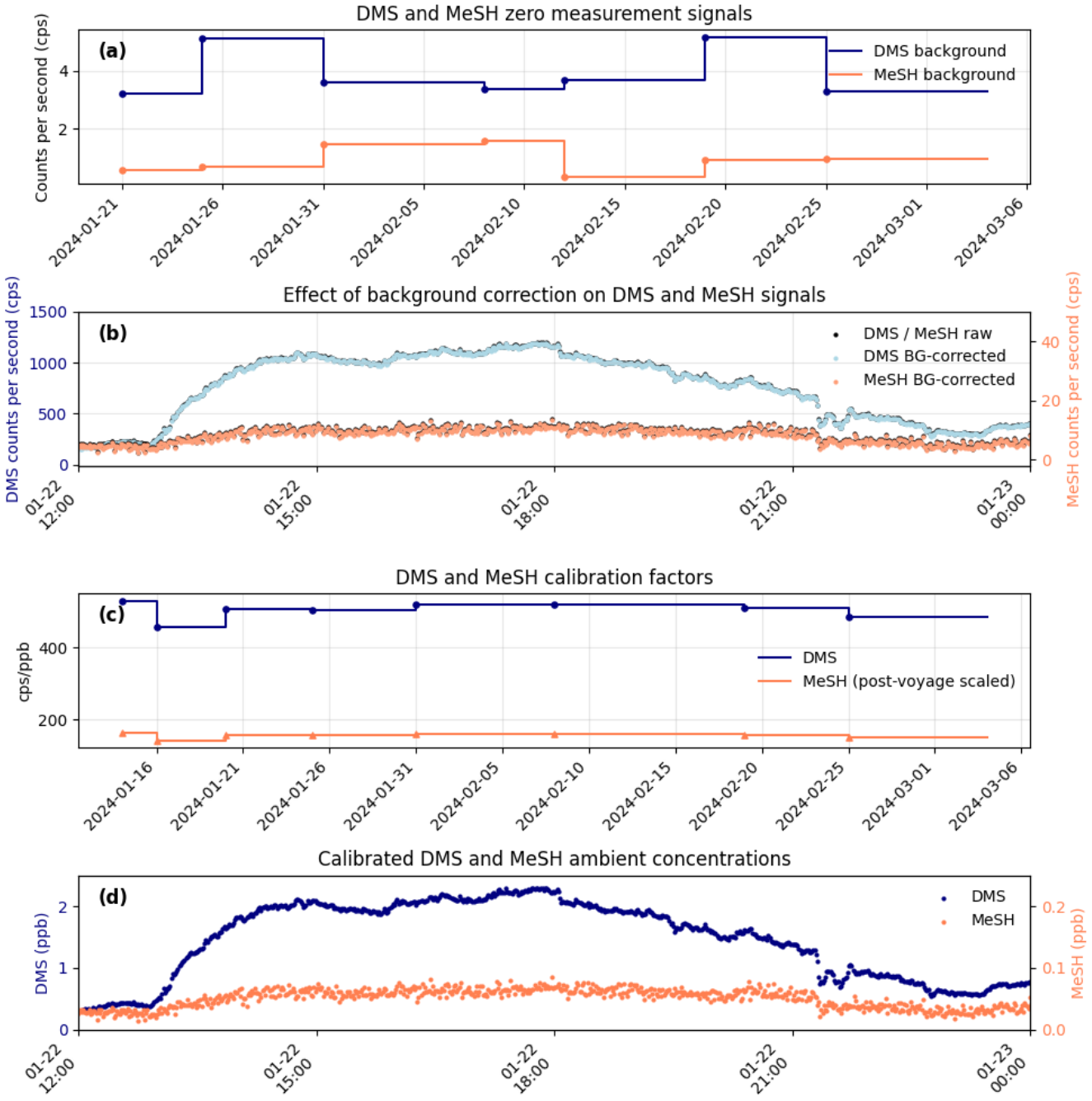

Figure S19. Calibration factors and background correction during the MISO voyage. (a) Zero measurements for DMS and MeSH, with step lines showing the forward-filled zero values applied to ambient measurements between zero measurement data points. (b) Example of the effect of background correction on raw DMS and MeSH ion signals over a representative 12-hour period. (c) DMS and MeSH calibration factors determined from gas standard calibrations throughout the voyage, with step lines indicating the calibration factors applied between calibrations. (d) Example of calibrated ambient DMS and MeSH mixing ratios during the same period shown in panel (b).

References

Asher, E. C., Dacey, J. W. H., Jarniková, T., and Tortell, P. D.: Measurement of DMS, DMSO, and DMSP in natural waters by automated sequential chemical analysis, Limnology and Oceanography: Methods, 13, 451–462, https://doi.org/10.1002/lom3.10039, _eprint: https://aslopubs.onlinelibrary.wiley.com/doi/pdf/10.1002/lom3.10039, 2015.

Bevington, P. R., Robinson, D. K., Morris Blair, J., John Mallinckrodt, A., and McKay, S.: Data Reduction and Error Analysis for the Physical Sciences, Computers in Physics, 7, 415–416, https://doi.org/10.1063/1.4823194, 1993.

De Gouw, J. and Warneke, C.: Measurements of volatile organic compounds in the earth's atmosphere using proton-transfer-reaction mass spectrometry, Mass Spectrometry Reviews, 26, 223–257, https://doi.org/10.1002/mas.20119, publisher: John Wiley & Sons, Ltd, 2007.

Dunne, E., Galbally, I. E., Cheng, M., Selleck, P., Molloy, S. B., and Lawson, S. J.: Comparison of VOC measurements made by PTR-MS, adsorbent tubes-GC-FID-MS and DNPH derivatization-HPLC during the Sydney Particle Study, 2012: A contribution to the assessment of uncertainty in routine atmospheric VOC measurements, Atmospheric Measurement Techniques, 11, 141–159, https://doi.org/10.5194/amt-11-141-2018, publisher: Copernicus GmbH, 2018.

Fetterer, F., Knowles, K., Meier, W. N., Savoie, M., Windnagel, A., and Stafford, T.: Sea Ice Index. (G02135, Version 4). [Dataset]., https://doi.org/10.7265/A98X-0F50, 2025.

Hayward, A., Murray, T., Di Geronimo, S., Wright, S., Westwood, K., Khan, M. A., Gutierrez-Rodriguez, A., and Pinkerton, M.: Phytoclass, now with a GUI: point-and-click pigment chemotaxonomy (in press), Limnology and Oceanography Bulletin.

Hayward, A., Pinkerton, M. H., and Gutierrez-Rodriguez, A.: phytoclass: A pigment-based chemotaxonomic method to determine the biomass of phytoplankton classes, Limnology and Oceanography: Methods, 21, 220–241, https://doi.org/10.1002/lom3.10541, _eprint: https://aslopubs.onlinelibrary.wiley.com/doi/pdf/10.1002/lom3.10541, 2023.

Hayward, A., Pinkerton, M. H., Wright, S. W., Gutiérrez-Rodriguez, A., and Law, C. S.: Twenty-six years of phytoplankton pigments reveal a circumpolar Class Divide around the Southern Ocean, Communications Earth & Environment, 5, 92, https://doi.org/10.1038/s43247-024-01261-6, publisher: Nature Publishing Group, 2024.

Hayward, A., Wright, S. W., Carroll, D., Law, C. S., Wongpan, P., Gutiérrez-Rodriguez, A., and Pinkerton, M. H.: Antarctic phytoplankton communities restructure under shifting sea-ice regimes, Nature Climate Change, 15, 889–896, https://doi.org/10.1038/s41558-025-02379-x, publisher: Nature Publishing Group, 2025.

Heidemann, A. C., Westwood, K. J., Foppert, A., Wright, S. W., Klocker, A., Vives, C. R., Wotherspoon, S., and Bestley, S.: Drivers of phytoplankton distribution, abundance and community composition off East Antarctica, from 55-80°E (CCAMLR Division 58.4.2 East), Frontiers in Marine Science, 11, https://doi.org/10.3389/fmars.2024.1454421, 2024.

JCGM: JCGM (Joint Committee for Guides in Metrology) 100: 2008 Evaluation of measurement data - Guide to the expression of uncertainty in measurement., http://www.bipm.org/utils/common/documents/jcgm/JCGM_100_2008_E.pdf, 2008.

Lawson, S. J., Law, C. S., Harvey, M. J., Bell, T. G., Walker, C. F., De Bruyn, W. J., and Saltzman, E. S.: Methanethiol, dimethyl sulfide and acetone over biologically productive waters in the southwest Pacific Ocean, Atmospheric Chemistry and Physics, 20, 3061–3078, https://doi.org/10.5194/acp-20-3061-2020, publisher: Copernicus GmbH, 2020.

Marandino, C. A., De Bruyn, W. J., Miller, S. D., and Saltzman, E. S.: Eddy correlation measurements of the air/sea flux of dimethylsulfide over the North Pacific Ocean, Journal of Geophysical Research: Atmospheres, 112, https://doi.org/10.1029/2006JD007293, _eprint: https://agupubs.onlinelibrary.wiley.com/doi/pdf/10.1029/2006JD007293, 2007.

Martínez-García, A., Oller, I., Vincent, M., Rubiolo, V., Asiimwe, J. K., Muyanja, C., McGuigan, K. G., Fernández-Ibáñez, P., and Inmaculada Polo-López, M.: Meeting daily drinking water needs for communities in Sub-Saharan Africa using solar reactors for harvested rainwater, Chemical Engineering Journal, 428, 132 494, https://doi.org/10.1016/j.cej.2021.132494, 2022.

McCulloch, R. and Tortell, P.: The determination of dimethyl sulfoxide in natural waters using electrochemical reduction, Limnology and Oceanography: Methods, 21, 529–541, https://doi.org/10.1002/lom3.10562, _eprint: https://aslopubs.onlinelibrary.wiley.com/doi/pdf/10.1002/lom3.10562, 2023.

Mynard, C., Franklin, E. B., Alroe, J., Somerville, N., Patti, A., Siems, S. T., Williams, A., Mallet, M. D., Humphries, R., and Dunne, E.: Constraining Atmospheric Methanethiol Estimates Over the Southern Ocean, Geophysical Research Letters, 52, e2025GL116 470, https://doi.org/10.1029/2025GL116470, _eprint: https://agupubs.onlinelibrary.wiley.com/doi/pdf/10.1029/2025GL116470, 2025.

Müller, M., Mikoviny, T., Jud, W., D'Anna, B., and Wisthaler, A.: A new software tool for the analysis of high resolution PTR-TOF mass spectra, Chemometrics and Intelligent Laboratory Systems, 127, 158–165, https://doi.org/10.1016/J.CHEMOLAB.2013.06.011, publisher: Elsevier, 2013.

Nagahata, T., Kajiwara, H., Ohira, S.-I., and Toda, K.: Simple Field Device for Measurement of Dimethyl Sulfide and Dimethylsulfoniopropionate in Natural Waters, Based on Vapor Generation and Chemiluminescence Detection, Analytical Chemistry, 85, 4461–4467, https://doi.org/10.1021/ac303803w, publisher: American Chemical Society, 2013.

Rocco, M., Dunne, E., Salignat, R., Saint-Macary, A., Peltola, M., Barthelmeß, T., Chamba, G., Barr, N., Safi, K., Marriner, A., Deppeler, S., Rose, C., Uitz, J., Harnwell, J., Engel, A., Colomb, A., Saiz-Lopez, A., Harvey, M. J., Law, C. S., and Sellegri, K.: Relating Dimethyl Sulphide and Methanethiol Fluxes to Surface Biota in the South-West Pacific Using Shipboard Air-Sea Interface Tanks, Journal of Geophysical Research: Atmospheres, 130, e2024JD041 072, https://doi.org/10.1029/2024JD041072, _eprint: https://onlinelibrary.wiley.com/doi/pdf/10.1029/2024JD041072, 2025.

Sekimoto, K., Li, S.-M., Yuan, B., Koss, A., Coggon, M., Warneke, C., and de Gouw, J.: Calculation of the sensitivity of proton-transfer-reaction mass spectrometry (PTR-MS) for organic trace gases using molecular properties, International Journal of Mass Spectrometry, 421, 71–94, https://doi.org/10.1016/j.ijms.2017.04.006, 2017.

Wright, S. W., van den Enden, R. L., Pearce, I., Davidson, A. T., Scott, F. J., and Westwood, K. J.: Phytoplankton community structure and stocks in the Southern Ocean (30–80°E) determined by CHEMTAX analysis of HPLC pigment signatures, Deep Sea Research Part II: Topical Studies in Oceanography, 57, 758–778, https://doi.org/10.1016/j.dsr2.2009.06.015, 2010.

Zang, C. L. and Willis, M. D.: Deployment and evaluation of an NH4+ H3O+ reagent ion switching chemical ionization mass spectrometer for the detection of reduced and oxygenated gas-phase organic compounds, Atmospheric Measurement Techniques, 18, 17–35, https://doi.org/https://doi.org/10.5194/amt-18-17-2025, 2025.